Article:
Wittkop, C, Swanner, ED, Grengs, A et al. (6 more authors) (2020) Evaluating a primary carbonate pathway for manganese enrichments in reducing environments. Earth and Planetary Science Letters, 538. 116201. ISSN 0012-821X

https://doi.org/10.1016/j.epsl.2020.116201

Manuscript for Earth and Planetary Science Letters

Title: Evaluating a primary carbonate pathway for manganese enrichments in reducing environments

Authors: Chad Wittkop*(1), Elizabeth D. Swanner (2), Ashley Grengs (1), Nicholas Lambrecht (2), Mojtaba Fakhraee (3), Amy Myrbo (4), Andrew W. Bray (5), Simon W. Poulton (5), and Sergei Katsev (3,6)

*Corresponding author, chad.wittkop@mnsu.edu, 507-389-6929

(1)Department of Chemistry and Geology, Minnesota State University, 241 Ford Hall, Mankato, MN 56001

(2)Department of Geological and Atmospheric Sciences, Iowa State University, 2337 Osborn Drive, Ames, IA, 50011

(3)Large Lakes Observatory, University of Minnesota Duluth 2205 East 5th Street, Duluth, MN 55812

(4) St. Croix Watershed Research Station, Science Museum of Minnesota, 16910 152nd St North, Marine on St. Croix, MN 55047 (5) School of Earth and Environment, University of Leeds, Leeds LS2 9JT, UK

(6)Department of Physics, University of Minnesota Duluth, 1049 University Drive, Duluth, MN 55812

Abstract

Most manganese (Mn) enrichments in the sedimentary rock record are hosted in carbonate minerals, which are assumed to have formed by diagenetic reduction of precursor Mn-oxides, and are considered diagnostic of strongly oxidizing conditions. Here we explore an alternative model where Mn-carbonates form in redox-stratified water columns linked to calcium carbonate dissolution. In ferruginous Brownie Lake in Minnesota, USA, we document Mn-carbonates as an HCl-extractable phase present in sediment traps and in reducing portions of the water column. Mn-carbonate become supersaturated in the Brownie Lake chemocline where dissolved oxygen concentrations fall below 5 μM, and Mn-oxide reduction increases the dissolved Mn concentration. Supersaturation is enhanced when calcite originating from surface waters dissolves in more acidic waters at the chemocline. In the same zone, sulfate reduction and microaerobic methane oxidation add dissolved inorganic carbon (DIC) with negative $\delta^{13}C$. These observations demonstrate that sedimentary Mn enrichments may 1) develop from primary carbonate phases, and 2) can occur in environments with dissolved oxygen concentrations <5 μM. Primary Mn-carbonates are likely to originate in environments with high concentrations of dissolved Mn (>200 μM), and where Mn and Fe are partitioned by S cycling, photoferrotrophy, or microaerophilic Fe-oxidation. A shallow lysocline enhances Mn-carbonate production by providing additional DIC and nucleation sites for crystal growth. This carbonate model for Mn-enrichments is expected to be viable in both euxinic and ferruginous environments, and provides a more nuanced view

of the relationships between Mn and carbon cycling, with applications throughout the rock record.

Word count

6483/6500 (1/14/20)

1. Introduction

The strong oxidizing potential (E = 1.228 V) required to form insoluble Mn(IV) oxides (e.g. MnO_2, pyrolusite) from reduced and dissolved Mn(II) make sedimentary Mn enrichments (SMEs) a proxy for the accumulation of oxygen in Earth's early atmosphere and oceans (Kirschvink et al., 2000; Planavsky et al., 2014). The world's largest SMEs occur in association with the Great Oxidation Event (GOE, 2.42-2.31 Ga; Gumsley et al., 2017), but large SMEs persist throughout the geologic record and are broadly correlated with known fluctuations in Earth's redox balance (Figure 1; Maynard, 2010).

Manganese (II)-carbonates are the most common minerals in SMEs, occurring primarily as rhodochrosite ($MnCO_3$), with lesser amounts of the dolomite group mineral kutnohorite ($CaMn[CO_3]_2$) and Mn-enriched calcite (Maynard, 2010; Johnson et al., 2016). These carbonates consistently bear negative carbon isotope signatures (e.g. Tsikos et al., 2010; Johnson et al., 2013), which are conventionally viewed to indicate diagenetic reduction (via microbial dissimilatory respiration) of precursor Mn(III/IV)-oxides in sediment porewater (Calvert and Pederson, 1996).

While this diagenetic pathway for Mn-carbonate genesis is favored by most recent investigators, the implication of precursor Mn-oxides can be controversial. Johnson et al. (2013) proposed that a 2.42 Ga SME originated from Mn-oxides formed by a hypothetical Mn-oxidizing photoautotroph. However, these SMEs have alternatively been viewed as evidence for O_2 accumulation prior to, or at the onset, of the GOE (e.g. Ossa Ossa et al., 2018), or direct deposition of Mn-carbonates from a stratified water column (Herndon et al., 2018). Archean SMEs are particularly problematic to explain, but may represent the emergence of oxygen oases prior to the GOE (e.g. Planavsky et al., 2014), direct precipitation of Mn-carbonates from seawater (Farquhar et al., 2014), or Mn-oxidation by a consortia of anoxygenic phototrophs (Daye et al., 2019)

Although less commonly invoked in recent interpretations of SMEs, alternative pathways for Mn-carbonate genesis are feasible in the low-O_2 settings observed in modern redox-stratified environments (Force and Cannon, 1988). These include anaerobic metabolisms that generate dissolved inorganic carbon (DIC), increases in pH that favor carbonate saturation (Rincon-Tomas et al., 2016), or nucleation on Ca-carbonates (Herndon et al., 2018). Consistent with this view, Mn-carbonates have been observed in association with reducing conditions in redox-stratified lakes (Nuhfer et al., 1993; Stevens et al., 2000; Jones et al., 2011).

While many lines of evidence converge on the necessity for direct Mn-carbonate precipitation from redox-stratified water columns, few detailed evaluations of the processes governing this pathway are available, particularly from ferruginous analogs for Archean and Proterozoic marine settings (e.g. Crowe et al., 2011). This is exacerbated by

90 the weak carbonate saturation of modern ferruginous lakes (the main analogs for ancient
91 ferruginous oceans) relative to marine environments.
92 In this work we investigate a recently described ferruginous meromictic lake
93 (Brownie Lake in Minnesota USA), which hosts both high dissolved Mn concentrations
94 (up to 130 μM) and supersaturation of key carbonate phases, to assess Mn-mineralization
95 pathways of relevance to anoxic environments across geologic time. We utilize this
96 setting to evaluate the hypothesis—most recently advanced by Herndon et al. (2018)—
97 that Mn carbonates may nucleate in the water column of redox stratified lakes. Here we
98 describe the biogeochemical reactions occurring under ferruginous conditions that drive
99 Mn-carbonate precipitation, and constrain the oxygen concentrations under which these
100 processes occur. We then use this framework to assess the potential for anoxic Mn-
101 carbonate genesis in the rock record, and evaluate the range of processes which may
102 contribute to the carbonate carbon isotope signatures of these deposits.
103
104
105 **2. Study site and methods**
106
107 Brownie Lake (BL) is a small ferruginous lake located in Minnesota, USA. The general
108 biogeochemistry of the site is described in Lambrecht et al. (2018), and Lambrecht et al.
109 (2020) presented a detailed study of its methane (CH_4) cycle. Water column profiling,
110 water sampling and analysis, and geochemical modeling were performed using routine
111 techniques detailed these publications and in our Supplementary Materials.

To assess Mn-phases in the water column, we analyzed particulate material from water column filtration and sediment traps from intervals representing a transition from oxic (shallower) to anoxic (deeper) conditions. Particulates were collected on 0.2 μM filters in August 2018 from 4.5, 7, and 10 m depth. Water column sediment traps (at 3.5, 5, and 11 m depth) were deployed from June through October 2018. Surface sediment samples were also collected in August 2018. Particulate and sediment samples were processed anaerobically as detailed in Supplementary Materials.

Particulate and sediment samples were freeze-dried and Mn was extracted from 50-100 mg of material using 10 mL of 0.5 M HCl for 1 hour, which targets reactive Mn^{2+} and some Fe (Thamdrup et al., 1994; Supplementary Materials). Manganese in the extractants, as well as total Mn and Al from sediment traps and surface sediments, were quantified by Atomic Absorption Spectrometry (Thermo Scientific iCE3000 series), with an RSD of less than 2.1% for all measurements. Sediment trap and surface sediment samples were further analyzed by X-ray diffraction (XRD), as detailed in Supplementary Materials.

To assess the relationships between carbonate phases and water column conditions, we developed scenarios in Geochemist's Workbench (GWB) utilizing BL water chemistry from the depths that displayed the greatest degree of Mn-carbonate saturation (May 2017 at 6 m; July 2017 at 5.5 and 6 m). At these intervals we considered a range of inorganic and biological processes that have previously been suggested to occur at a ferruginous chemocline, including phototrophy, methanotrophy, sulfate (SO_4^{2-}) reduction, and Ca-carbonate dissolution. A full description of our modeling approach can be found in Supplementary Materials.

3. Results

3.1 Manganese and carbon cycling in ferruginous Brownie Lake

Multi-year water column monitoring of BL demonstrates a stable, redox-stratified, ferruginous water column, with a chemocline depth (steep concentration gradient of water column solutes) of 4.5 m and a maximum depth of 14 m (Lambrecht et al., 2018; Figure 2). Dissolved O_2 concentrations were as high as 402 μM at 1 m depth in April 2017, while values below detection (~3 μM) were reached at depths of 3.5 m in July 2017 and 5 m in October 2015 (Figure 2 a). Concentrations of dissolved Fe, Mn, and SO_4^{2-} follow trends observed in many redox stratified environments (Figure 2 b-d), with dissolved Mn (interpreted as Mn^{2+}) first increasing at the chemocline to a maximum concentration of 134 μM at 4.5 m in October 2015. Sulfate was present above the chemocline, with a maximum concentration of 377 μM at 4 m in October 2015 (not plotted); samples collected in later visits reached a maximum of 122 μM at 2 m in April 2017, but were more typically between 20-40 μM above the chemocline in 2017. Sulfide concentrations were more variable, with a maximum value of 74 μM recorded at 5 m in September 2017. Dissolved Fe (interpreted as Fe^{2+}) consistently accumulated below the zones of dissolved Mn maxima and SO_4^{2-} drawdown, and rapidly increased below 6 m, with a maximum value of 1430 μM at 13 m recorded in July 2017.

157 The concentration of DIC ranged from 1.62 mM in surface waters to 14.05 mM at
158 depth, and generally followed the same pattern of increasing concentration with depth
159 regardless of the date measured (Figure 2 e). The $\delta^{13}C_{DIC}$ ranged from -12.87‰ (5 m
160 depth, September 2017) to a maximum of -1.97‰ at 12 m depth in May 2017. Regardless
161 of the date visited, the lowest $\delta^{13}C_{DIC}$ values were found near the chemocline, with
162 highest values at depth, and intermediate values in surface water (Figure 2 f).
163 Dissolved CH_4 concentrations were low near the surface (minimum 2.4 µM at 1 m
164 depth April 2017) and increased to 1555 µM at depth (12 m, September 2017). Dissolved
165 $\delta^{13}C_{CH4}$ ranged from -64.81‰ (5 m depth, September 2017) to values as high as -21.32‰
166 (4.5 m in May 2017; Figure 2 h inset). The $\delta^{13}C_{CH4}$ remained between -60 and -64‰
167 below the chemocline, and increased as dissolved CH_4 concentrations decreased
168 (Lambrecht et al., 2020).
169
170 *3.2 Brownie Lake pH and mineral solubility*
171
172 Profiles for pH in 2017 (Figure 3 a) demonstrate features consistent with stratification, as
173 well as seasonal changes. Surface water pH was generally higher than in deep water,
174 rising as high as 8.85 in May 2017. Lowest pH values were observed below the
175 chemocline late in the summer, with values as low as 6.26 observed in September 2017.
176 The pH decrease across the chemocline was smaller in summer months, as demonstrated
177 by the nearly identical pH profiles in May and July.
178 Surface water samples showed slight calcite supersaturation (Figure 3 b,
179 maximum SI = 0.69 in April 2017; SI = saturation index or Q/K where Q = ion activity

product, and K = given mineral solubility constant), with undersaturation observed in deeper waters (SI = -1.12 at 9 m depth in September 2017). Below the chemocline the Mn-carbonate phases pseudokutnahorite (max SI = 3.48 at 6 m depth, July 2017) and rhodochrosite (max SI = 0.46 at 6 m depth, July 2017) became supersaturated (Figure 3 c). As DIC and Fe^{2+} accumulated in the deepest waters, siderite ($FeCO_3$) also became supersaturated, with a maximum SI of 1.58 observed at 13 m in July 2017 (Figure 3 b). A closer examination of the key carbonate phases across the 2017 sampling dates (Figure 3 c) suggests that Mn-carbonate saturation varied throughout the summer, while calcite and siderite remained saturated in surface and deep waters, respectively.

Major Fe and Mn oxide phases were supersaturated in surface waters but became strongly undersaturated in anoxic waters (Lambrecht et al., 2018). The solubility of phosphate phases in BL is discussed in Supplementary Materials.

3.3 Particulate and sediment geochemistry

Figure 4 displays solid phase Mn data and carbonate mineralogy from three sources in BL: filtered particulates, sediment traps, and surface sediments. The HCl-extractable Mn fraction ranged from 862 ppm from the 3.5 m sediment trap, to 189 ppm from a particulate sample filtered from 10 m depth. The ratio of HCl-extractable Mn to total Mn in sediment trap and surface sediment samples ranged from 0.070 to 0.085, while total Mn/Al in these samples ranged from 0.021 to 0.032, with the highest values in both measures deriving from the 3.5 m sediment trap sample (Figure 4). Sediment trap

materials from 5 m displayed more intense XRD peaks for calcite than did surface sediments.

3.4 Geochemical modeling

A process sensitivity analysis and results of simulations for three Mn-carbonate saturated BL intervals are shown in Figure 5, with model inputs shown in Table 1. After considering a broader range of potential processes that might influence carbonate saturation at a ferruginous chemocline (Supplementary Materials), we identified key relationships in the sensitivity analysis for the July 2017 5.5 m interval (the most strongly Mn-carbonate supersaturated in our study) that governed the carbonate saturation behavior of all of our simulations. The first two simulations assessed the role of aerobic organic carbon respiration (AR) versus aerobic CH_4 oxidation (MO):

(1) $CH_2O + O_2 = CO_2 + H_2O$ (AR)

(2) $CH_4 + 2O_2 = CO_2 + 2H_2O$ (MO)

The key difference between the two processes is the molar ratio of O_2 consumed to CO_2 produced: 1:1 for AR, and 2:1 for MO. Both scenarios had the same impact on carbonate saturation. The greater impact of these processes was the removal of O_2, which even at the very low concentrations observed in the upper chemocline of BL appears to inhibit Fe^{2+} activity in the model. Complete O_2 removal enhanced Fe^{2+} activity and

created a subtle boost in siderite saturation (+0.4 Q/K) in both scenarios, with no other observable differences.

Next we considered sulfate reduction (SR), which adds 2 moles of HCO_3^- for each mole of SO_4^{2-} consumed.

(3) $SO_4^{2-} + 2CH_2O = H_2S + 2HCO_3^-$ (SR)

Sulfate reduction had a subtle impact on carbonate saturation, with siderite showing the greatest increase (~0.6 Q/K), followed by rhodochrosite (~0.2 Q/K) then calcite; the greatest changes occurred in the first two days of the simulation.

Next we assessed the addition of calcite at a rate consistent with surface water calcite saturation from July 2017 (Supplementary Materials). Calcite addition had the greatest impact on rhodochrosite solubility during the simulation, increasing it by 1.5 Q/K. Calcite solubility had a more subtle response, increasing by only 0.5 Q/K, while siderite solubility experienced no change in this scenario.

The remaining panels in Figure 5 display the impact of the combined processes (MO, SR, and calcite addition) with varying temperature and pH. Increasing temperature in the system to 25°C resulted in modest increases in mineral saturation, though the relative changes are the same for each mineral. Increasing the system pH from 7 to 8.5 resulted in significant increases in mineral saturation, particularly between pH 7.5 and 8. At the highest pH (8.5), siderite experienced nearly the same increase in Q/K as rhodochrosite.

A final series of scenarios (Figure 5 i-l) considered a solution based on BL dissolved Fe, Mn, O_2, and SO_4 values, and adopting modern seawater concentrations for the remaining ions at pH 8 and a temperature of 25°C. In the first scenario with dissolved Mn concentration from the BL July 5.5 m interval (Figure 5 i), calcite saturation increased more than rhodochrosite. However, increasing dissolved Mn concentration in subsequent seawater scenarios led to significant increases in rhodochrosite Q/K (~+15), with the maximum observed increase corresponding to a Ca:Mn of 18, which was the highest observed in BL.

Figure 6 shows the impacts of combined SR, MO, and calcite addition on carbonate mineral saturation from three BL intervals: May 2017 at 6 m, and July 2017 at 5.5 and 6 m, as detailed in Table 1. The results are shown for both mineral precipitation suppressed (as delta Q/K) and unsuppressed (μmol precipitated) scenarios, as well as the response in system pH through the course of each simulation.

In each suppressed scenario (Figure 6 a-c) rhodochrosite saturation increased the most, followed by siderite, while calcite saturation increased linearly throughout the simulation. Siderite saturation displayed a similar pattern in each scenario, with an initial sharp increase followed by a more gradual climb, and siderite saturation increased nearly as much as rhodochrosite in the July 2017 6 m scenario (Figure 6 b). In these scenarios pH gradually increased in each case (Figure 6 d-f)

Unsuppressed scenarios demonstrated key differences in the proportions of minerals produced by these simulations (Figure 6 g-i). One scenario created more calcite than rhodochrosite, the second created a mixture of the three minerals, and the last

precipitated only rhodochrosite. In unsuppressed scenarios, pH changes were generally more muted (Figure 6 j-i), and system pH was lower overall.

4. Discussion

4.1 Manganese and carbonate cycling in Brownie Lake

Reactive particulate (HCl-extractable) Mn, representative of carbonate-associated Mn, was present in BL only below the seasonal oxycline (~3.5 m), and represented a consistent fraction of total anoxic sediment Mn (Figure 4 c.). Coupled with XRD evidence for calcite dissolution below the BL chemocline (Figure 4 d.), we suggest this phase most likely consists of calcite crystals precipitated in surface waters, which became encrusted with Mn-enriched rims during water column settling, resulting in crystals similar to those previously documented in lake sediments (Stevens et al., 2000; Herndon et al., 2018).

Although we cannot eliminate the possibility that some HCl-extractable Mn in BL was associated with a non-carbonate phase, such as a poorly crystalline sulfide or phosphate (see discussion in Supplementary Materials), it is unlikely to represent Mn-oxides. Mn-oxides are thermodynamically unstable in ferruginous BL as their reduction is rapidly coupled to the oxidation of Fe(II), sulfide, ammonium and CH_4 (e.g. Jones et al., 2011), all of which are present in BL waters (Lambrecht et al. 2018; Figure 2). Furthermore, while HCl-extractable Mn was associated with Mn-oxide phases in

292 ferruginous Lake Matano, this was for samples containing nm-scale oxide filaments
293 above the chemocline. By contrast, below the Matano chemocline Mn-oxides were
294 rapidly reduced and replaced by a phase with a XANES spectrum consistent with
295 rhodochrosite (Jones et al., 2011).

296 The dissolved Mn accumulation in the BL chemocline is among the most
297 concentrated reported in redox-stratified lakes (up to 134 μM), indicating the presence of
298 a vigorous Mn redox cycle (e.g. Jones et al., 2011; Herndon et al. 2018). Microbial Mn^{2+}
299 oxidation may contribute to Mn cycling within the BL chemocline, where it is known to
300 operate efficiently within the O_2 concentration gradients (~3-30 μM) observed there
301 (Clement et al., 2009). Seasonal dynamics of the BL Fe and S cycles may also contribute
302 to the dissolved Mn pool, as late season sulfide generation by SR drives removal of
303 dissolved Fe, increasing dissolved Mn:Fe at the top of the chemocline.

304 Water column pH decreased with depth but stabilized at the chemocline before
305 reaching its lowest values in the deepest waters (Figure 3). This zone of pH stability at
306 the chemocline was likely driven by a number of processes buffering the overall decline
307 in pH with depth. For example, Mn-oxide reduction raises pH when coupled to organic
308 carbon, sulfide, or CH_4 oxidation (Jones et al., 2011; Johnson et al., 2013):
309
310 (4) $CH_2O + 2MnO_2 + 2H^+ = CO_3^{2-} + 2Mn^{2+} + 2H_2O$
311
312 (5) $H_2S + 4MnO_2 + 2H_2O = SO_4^{2-} + 4Mn^{2+} + 6OH^-$
313
314 (6) $CH_4 + 4MnO_2 + 7H^+ = HCO_3^- + 4Mn^{2+} + 5H_2O$

315

316 Of these processes, we consider reactions 4 and 5 most likely to be active at the
317 BL chemocline, based on the concentrations of species present and the eutrophic nature
318 of the lake (Lambrecht et al., 2020), which provides a large reservoir of organic carbon to
319 the system. Similar to reaction 4, iron reduction coupled to organic carbon oxidation is
320 also capable of decreasing acidity (Walter et al., 2014). While experiments confirm that
321 reaction 6 can be microbially mediated (Ettwig et al., 2016), organisms putatively
322 capable of such a reaction were in very low abundance (Lambrecht et al., 2020), and
323 reaction thermodynamics seem unlikely to support such organisms in BL.
324 Pelagic calcite dissolution, a well-known processes in seasonally stratified lakes
325 (e.g. Myrbo and Shapley, 2006), may further serve to influence pH and DIC changes at
326 the chemocline, via:
327
328 (7) $CaCO_3 + H^+ = Ca^{2+} + HCO_3^-$
329
330 or by uptake of CO_2 released through reactions 1 and 2:
331
332 (8) $CaCO_3 + CO_2 + H_2O = Ca^{2+} + 2HCO_3^-$
333
334 Our solubility calculations (Figure 3), the reduction in intensity of the calcite
335 XRD peaks between the sediment trap and surface sediments (Figure 4), and the
336 enrichment in dissolved Ca in the deep waters of BL (Lambrecht et al., 2018), are all
337 consistent with calcite dissolution occurring near the chemocline.

Surface levels of BL carbonate saturation and changes across the chemocline are similar to those recently documented in euxinic Green Lake, NY (Herndon et al., 2018), but key differences emerge in the deep ferruginous waters of BL. In Green Lake, rhodochrosite was only supersaturated in a narrow zone around the chemocline. In BL, rhodochrosite was supersaturated at and below the chemocline, and siderite became supersaturated in deep ferruginous waters. This would enable continued Mn-carbonate crystal growth in deep water, with potential for incorporating Fe into carbonates where bottom waters are saturated in siderite.

Carbonate crystals likely spend sufficient time in Mn-enriched waters to incorporate significant Mn^{2+}. Stokes settling times (at 25° C) for 5 μm crystals through a non-turbulent, 1.5 m chemocline are on the order of several hours, and increase exponentially for smaller crystals. Experimental studies (e.g. Pingitore et al., 1988) suggest Mn^{2+} uptake by calcite is favored at slower precipitation rates that would nonetheless generate significant amounts of Mn-carbonates at these settling velocities (e.g. 200 $\mu g\ min^{-1}\ m^{-2}$). Hence Mn-carbonate precipitation would be favored in an environment where μm-scale crystals settle for several hours or more, and remain in contact with rhodochrosite supersaturated waters at the sediment-water interface, as is observed in BL (Figure 3).

4.2 Controls on carbonate solubility in Brownie Lake

Our sensitivity analysis demonstrates that calcite addition has the greatest impact on rhodochrosite saturation in BL (Figure 5). This is likely driven by the relative solubilities of the two minerals, with more soluble calcite (pK = 8.48 vs. rhodochrosite pK = 10.08,

361 Morse et al., 2007) dissolving at the chemocline and contributing bicarbonate to the
362 system (eq. 8). The sensitivity of the system to increases in rhodochrosite saturation
363 appears to be further governed by increasing dissolved Mn concentration (up to 400 μM),
364 pH, and temperature. As Fe concentrations increase, such as below the chemocline,
365 siderite becomes an significant component of the system.

366 Sulfate reduction at the BL chemocline also holds the potential to influence
367 carbonate saturation. Despite generally low SO_4^{2-} concentrations, SR is active in BL
368 waters, consistent with other ferruginous lakes where vigorous sulfur cycling occurs
369 (Walter et al., 2014). Because SR generates two mol of HCO_3^- for each mol of SO_4^{2-}
370 reduced (eg. 3), this process drove an initial spike in Fe-Mn carbonate saturation in our
371 modeled intervals (e.g. Figure 5 c).

372 Unsuppressed scenarios (Figure 6) show that subtle variations in water Mn:Fe and
373 pH can produce carbonate assemblages with highly variable proportions of Ca-Mn-Fe,
374 consistent with many ancient examples of Mn enrichments where both Mn-Ca and Mn-Fe
375 carbonates are reported (Tsikos et al., 2010; Johnson et al., 2016; Planavsky et al. 2018).
376 Although the assumption of siderite precipitation at 1-fold saturation may be unrealistic
377 in these scenarios, nucleation on existing crystals may lower the kinetic barriers to
378 precipitation relative to homogeneous phases (Jiang and Tosca, 2019). Experimental
379 work previously implicated calcite as a catalyst in Mn-carbonate precipitation. Mucci
380 (2004) suggested Mn-carbonate minerals could nucleate on small calcite crystals, or
381 manifest as manganoan rims on calcite if concentrations of Ca^{2+} were much greater than
382 Mn^{2+}.

These scenarios translated well to manganiferous seawater with minor adjustments. Increasing temperature and pH favored carbonate production (Figure 5 e-h), but an initial seawater scenario (Figure 5 i) illuminated a challenge to the model: competition between calcite and rhodochrosite at marine concentrations of Ca. The molar Ca:Mn of BL water in our sensitivity scenarios derives from a measured value of 25.6, but scaling to marine Ca increases this ratio to 138 (Table 1). Adjusting the dissolved Mn concentration of the seawater scenarios to include the highest measured concentration observed in this study (134 μM) led to greater increases in rhodochrosite saturation, consistent with BL scenarios. Subsequent seawater scenarios with 200 μM dissolved Mn, and a Ca:Mn ratio adjusted to the lowest observed in BL (~18 or a dissolved Mn concentration of 571 μM) generated considerable increases in rhodochrosite saturation relative to calcite, demonstrating the viability of this mechanism in marine settings. Although the final scenario had a dissolved Mn concentration over 4-fold larger than we observed in BL, it is not an unreasonably high concentration for a marine system given the dissolved Mn concentrations of >400 μM reported in the modern Orca Basin (Van Cappellen et al., 1998).

4.3 Dissolved inorganic carbon isotopes in redox-stratified waters

Differences in $\delta^{13}C_{DIC}$ behavior between euxinic versus ferruginous waters largely derive from the prominence of the CH_4 cycle in ferruginous systems. Although modern ferruginous lakes occur in a variety of hydroclimatic settings, data presented here (Figure 2) reinforce the observation that these systems display stratification in $\delta^{13}C_{DIC}$.

406 Ferruginous chemoclines host lower $\delta^{13}C_{DIC}$ relative to deep waters that are influenced by
407 fermentation or methanogenic CO_2 reduction (Assayag et al., 2008; Crowe et al., 2011;
408 Lambrecht et al. 2020; Figure 2). Calcite dissolution also holds potential to contribute
409 heavier DIC to deep waters (Myrbo and Shapley, 2006). In contrast, euxinic lakes also
410 demonstrate a more common mode of $\delta^{13}C_{DIC}$ stratification, wherein waters from the
411 chemocline and below reflect light $\delta^{13}C_{DIC}$ release from AR and SR of organic carbon
412 (Myrbo and Shapley, 2006; Havig et al., 2017; Figure 7).
413
414 *4.3.1 Impact of methane oxidation on Brownie Lake DIC*
415
416 A pronounced depletion in $\delta^{13}C_{DIC}$ at the chemocline and progressive enrichment through
417 deep anoxic waters reflect active CH_4 cycling in the BL water column, with oxidation at
418 the chemocline, and methanogenesis in deep anoxic waters (Lambrecht et al., 2020;
419 Figure 2 e & f). The increase towards positive $\delta^{13}C$-CH_4 consistent with methanotrophy
420 occurs at the base of the oxycline, at O_2 concentrations between 4-5 μM. While SO_4-
421 dependent anaerobic oxidation of CH_4 (AOM) is marginally thermodynamically
422 permissible in this context, BL 16S rRNA sequencing recovered negligible sequences of
423 putative AOM archaea (Lambrecht et al., 2020). This is consistent with recent work
424 demonstrating that aerobic methanotrophy remains favored in ferruginous systems even
425 at oxygen levels below the detection limit of most sensors (~ 20 nmol; Oswald et al.,
426 2016).
427 Both SR and MO are thermodynamically favored in BL (Supplementary
428 Materials), and capable of influencing $\delta^{13}C_{DIC}$. It is therefore necessary to consider which

process may be exerting a greater influence on BL DIC. Employing the reaction-diffusion approach developed by Crowe et al. (2011), and adopting the vertical eddy diffusivity value around the chemocline of BL on the order of $5x10^{-5}$ m^2/s (Lambrecht et al., 2018), we calculate that an MO rate of 160 μmol/L/day is required to maintain the negative DIC carbon isotope excursion observed at 4.5 m depth in September 2017. This is within the range of known lacustrine MO rates, and slightly higher than the maximum rate recently determined in ferruginous Lake Matano (Sturm et al., 2019). Although dissolved oxygen concentrations at this interval (~4.7 μM) were just above the detection limit of our sonde (2-3 μM), they would be sufficient to maintain aerobic CH_4 oxidation. This rate is also similar to the upward flux of CH_4 towards the chemocline, as calculated from the CH_4 concentration profile (90 μmol/L/day, assuming oxidation occurs over a 0.5 m interval), suggesting that the BL carbon isotope excursion could be maintained primarily by MO, though contributions to the pool of isotopically light DIC from other pathways is further evaluated below.

A mass balance of BL DIC data suggests MO has a stronger influence on the DIC excursion at the chemocline, with a ratio of ~3:1 MO:SR, consistent with its thermodynamic favorability (Supplementary Materials). Nitrate- and Fe-Mn-coupled AOM (Ettwig et al., 2016; Oswald et al., 2016) are intriguing but remote possibilities, considering such organisms were not significant in BL (Lambrecht et al. 2020). Concentrations of NO_3^- observed at Brownie Lake are generally <2 μM (Lambrecht et al., 2018) and are not likely to significantly impact the CH_4 budget. And although it has been demonstrated in experiments (Ettwig et al., 2016), a clear example of pelagic MO coupled to Fe/Mn oxide reduction has yet to be produced. Thus, this analysis suggests

452 that aerobic CH_4 oxidation may exert a major influence on $\delta^{13}C_{DIC}$ in Brownie Lake,
453 consistent with the suggestion that methanotrophy is a major influence on $\delta^{13}C_{DIC}$ in
454 ferruginous waters (Crowe et al., 2011).
455
456 *4.3.2 Methane oxidation and carbonate C isotopes*
457
458 The widespread observation of low $\delta^{13}C$ in Mn-carbonates is traditionally interpreted as
459 evidence of diagenetic oxide reduction coupled to organic carbon respiration within
460 sediments (e.g. Calvert and Pederson, 1996; Planavsky et al., 2018). While this
461 interpretation is viable in many geological examples, the influence of MO and SR on
462 $\delta^{13}C_{DIC}$ in ferruginous lakes demonstrates the potential for embedding signatures of these
463 processes in primary carbonate minerals.
464 Carbonates derived from CH_4 oxidation have long been recognized (Michaelis et
465 al., 2002) and are widely described in modern lacustrine and marine environments. In
466 marine settings, SO_4-AOM triggers precipitation of carbonates and sulfides (Michaelis et
467 al., 2002). In completely anoxic and ferruginous settings where SO_4^{2-} is below 10s of μM,
468 benthic archaea have been shown to couple both Fe and Mn-oxide reduction to CH_4
469 oxidation (Ettwig et al., 2016), a reaction that similarly favors carbonate precipitation
470 (Crowe et al., 2011).
471 Aerobic oxidation of CH_4 to CO_2 has a substantially lower redox potential relative
472 to Mn^{2+} oxidation, permitting CH_4 oxidation in suboxic environments where Mn^{2+} would
473 remain reduced (Supplementary Materials). Such a nuanced separation of these processes

474 is possible in a redox-stratified water column, but would be less likely to overlap in
475 sediments where oxygen would be unlikely to penetrate to a zone of methane production.
476 Earlier interpretations of $\delta^{13}C$ from iron formation carbonates suggested greater
477 variability in the $\delta^{13}C$ of marine DIC sources (e.g. Winter and Knauth, 1992), consistent
478 with the recent suggestion that signatures of hydrothermal DIC may be recorded by some
479 ancient Fe-carbonates (Jiang and Tosca, 2019). Although the interpretation of primary
480 versus diagenetic signatures of ancient carbonates remains subject to much debate, it is
481 clear that a number of primary processes operating in redox-stratified water columns may
482 generate substantial variability in $\delta^{13}C_{DIC}$.
483
484 *4.4 Mn-carbonates in anoxic environments*
485
486 Recent literature largely assumes that Mn burial in permanently anoxic basins is not
487 permissible due to the instability of Mn-oxides and high solubility of Mn-sulfides
488 (Calvert and Pederson, 1996). In the prevailing view, Mn-carbonates form in sediment
489 porewater after diagenetic reduction of Mn-oxides precipitated from water columns that
490 are at least episodically oxidized (e.g. Johnson et al., 2013). Our findings, however, are
491 consistent with work in both ferruginous (Jones et al., 2011) and euxinic lakes (Herndon
492 et al., 2018), supporting the hypothesis that primary precipitation of Mn-carbonates is
493 favorable in redox-stratified water columns containing 5 μM of oxygen or less.
494 Observations of Mn-carbonates in sediment traps (Nuhfer et al., 1993), water
495 column particulates (Jones et al., 2011), and Holocene sediments (Wittkop et al., 2014)
496 from redox-stratified lakes further support the existence of a primary precipitation

497 pathway. The Mn-carbonate phase documented in Elk Lake, Minnesota was not found in
498 sediment traps sterilized with formalin (Nuhfer et al., 1993), implicating microbial
499 processes in its precipitation (Stevens et al., 2000). Consistent with marine examples, the
500 lacustrine Mn-carbonate overgrowths on calcite crystals documented by Stevens et al.
501 (2000) corresponded to lighter bulk carbonate $\delta^{13}C$ than in intervals without Mn-
502 carbonates, consistent with a potential role for AR or MO in their origin.
503 This evidence also points to a relatively rapid precipitation of Mn-carbonates
504 within redox-stratified water columns. Rhodochrosite was identified by XRD in sediment
505 traps by Nuhfer et al. (1993), and in particulate samples by XANES in Lake Matano
506 (Jones et al., 2011). Pseudokutnohorite is thermodynamically favored to precipitate
507 before rhodochrosite (Mucci 2004), but to our knowledge this XRD-amorphous mineral
508 has not been reported in lacustrine settings, though Stevens et al. (2000) reported
509 kutnohorite in Holocene sediments.
510
511 *4.5 Application to ancient SMEs*
512
513 In light of the evidence presented here, we advance a primary carbonate model for the
514 genesis of SMEs (Figure 7 a). The key elements of the carbonate model are, 1) a redox
515 stratified basin hosting Mn-enriched waters near a redoxcline, 2) Ca-carbonate
516 precipitation in shallow waters, and 3) a lysocline poised near the basin redoxcline. While
517 our work demonstrates that this model may be especially viable in ferruginous
518 environments, it is also consistent with suggestions that Mn-carbonates may represent an
519 primary precipitate in euxinic settings (Force and Cannon, 1988; Herndon et al., 2018).

Most SMEs occur in shallow water facies (Force and Cannon, 1988), and secondary enrichment is precluded in key examples (e.g. Johnson et al., 2013), thus their genesis requires the presence of Mn-enriched waters in shallow marine environments, and hence a shallow chemocline. Substantial deposits require proximity to hydrothermal Mn sources (Maynard, 2010), which may dictate the Mn:Fe of basin waters, but additional Fe and Mn segregation may occur at a chemocline as observed in BL. Fe can be oxidized by anoxygenic photoferrotrophy in the photic zone (e.g. Lliros et al., 2015), or by microaerophilic Fe(II)-oxidizing bacteria (Berg et al., 2019). Both of these processes would increase dissolved Mn:Fe. A cryptic sulfur cycle may similarly proceed under weakly oxidizing conditions (e.g. Walter et al., 2014), leading to an increase in Mn:Fe via Fe-sulfide precipitation (Force and Cannon, 1988).

In contrast to the episodic mixing observed in seasonally-stratified lakes, a more stable marine environment would offer the advantage of maintaining the redox relationships observed in BL for longer periods of time, enhancing the potential for large-scale Mn mineralization. Basin upwelling events may introduce Mn-enriched waters to depositional sites, but many SMEs are also linked to marine transgressions (Roy, 2006). A transgression could lead to migration of a chemocline over previously deposited Ca-carbonates, where Mn-enriched waters would have the opportunity to act as a "mineralizing fluid" on surface sediments (Force and Cannon, 1988). Changes in sea level may also lead to interbedding of primary carbonates alongside Mn-oxides, which could later be diagenetically reduced, accounting for the complex mineral associations observed in major Mn enrichments (e.g. Johnson et al., 2016). Independent of eustatic sea

542 level, the chemocline may shift position in response to the relative supply of oxidants
543 versus reductants in seawater (e.g. Lantink et al. 2018).
544 Capture of Mn by carbonate phases may preclude large-scale oxide precipitation
545 if the rate of carbonate capture and burial equals or exceeds the rate of Mn supply to the
546 basin. In contrast, a large Mn-oxide deposit would indicate a rate of Mn upwelling and
547 oxidation exceeding the rate of capture by carbonates, or a transition to an environment
548 unfavorable for carbonate production or preservation.
549
550 *4.5.3 The carbonate pathway in Precambrian SMEs*
551
552 Sharp facies gradients between Ca-carbonates and ferruginous or manganiferous
553 sediments are present in many examples SMEs occurring both before and after the GOE
554 (e.g. Johnson et al., 2013; Lantink et al., 2018; Ossa Ossa et al., 2018b), implying the
555 presence of a basin lysocline. The lysocline in small temperate lakes such as BL is driven
556 primarily by temperature and rates of OM remineralization (e.g. Myrbo and Shapley,
557 2006). In ancient ferruginous basins, a shallow lysocline may have been further supported
558 by the presence of metal-enriched hydrothermal waters with a lower pH relative to
559 surface waters.
560 Recent estimates of dissolved O_2 concentrations derived from Archean SMEs are
561 higher than the 3-4 μM we considered in our BL simulations, but are generally consistent
562 with the 3-30 μM range we observe in manganiferous BL waters. The concentrations of
563 dissolved O_2 represented by Archean SME may have locally exceeded 10 μM (Ossa Ossa

564 et al., 2018), within a range that could support rapid microbial Mn^{2+} oxidation and further
565 concentrate dissolved Mn at a local chemocline (Clement et al., 2009).

566 Although Mn-oxides may be generated in some low-O_2 settings (e.g. Daye et al.
567 2019), the relationships between O_2 and manganiferous waters in BL imply that efficient
568 Mn-oxide burial would require O_2 concentrations at the sediment water interface to
569 remain significantly above 5 μM. We observed O_2 concentrations ranging between ~5-50
570 μM at the top of the BL chemocline where tens of μM of dissolved Mn began to
571 accumulate, indicating Mn-oxide reduction was occurring in these waters. Hence Mn
572 would remain dissolved in environments where O_2 may be present at <5μM—
573 concentrations that could nonetheless support Fe^{2+} and CH_4 oxidation. Here a carbonate
574 burial pathway for Mn^{2+} would remain viable, with the production of various Mn-
575 minerals dependent on reaction kinetics and the stability of redox gradients.

576 These interpretations are consistent with Fe-isotope evidence from the Hotazel
577 Formation of the Transvaal Supergroup, deposited near the onset of the GOE. Hotazel
578 records suggest SME genesis from a redox-stratified basin possessing a large reservoir of
579 dissolved Fe, and evolving Fe-Mn ratios (Lantink et al. 2018). A primary carbonate
580 model also accounts for the co-occurrence of Mn(II-III) and Fe(III) phases in Mn-
581 enrichments interpreted to represent a limited role for diagenetic reduction in the genesis
582 of Hotazel SMEs (Tsikos et al., 2010).

583 Manganese enrichments in deep water facies of the Proterozoic Animikie Basin
584 were recently interpreted as evidence of complete water column oxidation (Planavsky et
585 al. 2018), who invoked a Baltic Sea analog (e.g. Hausler et al., 2018). While the Baltic
586 Sea SMEs are consistent with deep water oxygenation and genesis from Mn-oxide

587 precursors, they also occur in an environment of very low Fe:Mn, which is not consistent
588 with the high Fe:Mn of the manganosiderite phases preserved in the Animikie examples
589 (Planavsky et al, 2018). A primary carbonate genesis of the Animikie examples followed
590 by continued Fe-carbonate growth on the seafloor (e.g. Figure 7 a.) is more consistent
591 with both previous work on the Animikie Basin (Poulton et al., 2010), and examples of
592 highly Mn-enriched Fe-carbonates preserved in ferruginous Holocene sediments
593 (Wittkop et al., 2014).

594 Although Mo isotope depletions are frequently interpreted as indicators of Mn-
595 oxide burial (e.g. Planavsky et al., 2018), they may also occur at a euxinic chemocline in
596 association with changes in Mo-S speciation (Neubert et al., 2008). The co-occurrence of
597 pyrite with Proterozoic SMEs (Johnson et al., 2013; Planavsky et al., 2018) supports this
598 view, and opens the possibility that some Precambrian SMEs contain records of cryptic S
599 cycling as opposed to complete water column oxidation.

600

601 *4.5.4 The carbonate pathway in Phanerozoic SMEs*

602

603 Manganese enrichments from the Neoproterozoic and younger are generally consistent
604 with more diverse mineralization pathways relative to older examples (Maynard, 2010).
605 Phanerozoic SMEs are frequently associated with black shales, whose sulfides represent
606 an effective Fe-sink, allowing for accumulation of dissolved Mn in the water column
607 (Force and Cannon, 1988). These younger SMEs may remain associated with large-scale
608 changes in marine redox balance, including ocean anoxic events, and the occurrence of
609 marine red-beds, which have recently been interpreted as evidence for transient

610 ferruginous episodes in the Phanerozoic (Figure 1; Song et al., 2017). Localized tectonic
611 influences may overprint this global signal, which is the likely case for the Oligocene
612 deposits associated with the Black Sea (Force and Cannon, 1988).
613 The Jurassic Molgano deposit of Mexico is the largest Phanerozoic SME,
614 occurring at the base of a Ca-carbonate facies (Okita, 1992), where it is tellingly not
615 associated with primary oxides (Force and Cannon, 1988). Instead, detailed mapping of
616 Mn-phases in Molgano samples suggests manganoan calcite may have represented the
617 earliest precipitate (Johnson et al., 2016). Other Phanerozoic examples including the
618 Oligocene Nikopol deposit of Ukraine and Cretaceous Groote Eylandyt deposit of
619 Australia contain Mn-carbonates associated with primary oxides. This co-occurrence of
620 adjacent oxide and carbonate SMEs within the same sedimentary basin likely represents
621 the preservation of a water column redox boundary (Force and Cannon, 1988). Careful
622 re-assessment of such Phanerozoic SMEs utilizing new paleoredox tools is likely to
623 provide insight into their relationships with global versus localized drivers of their
624 genesis.
625
626
627 **5. Conclusions**
628
629 We document the production and burial of an HCl-extractable particulate Mn phase,
630 interpreted as a Ca-Mn-carbonate, from a ferruginous Brownie Lake. Geochemical
631 models of carbonate production in the lake suggest introduction of calcite to Mn-rich
632 waters at the chemocline triggers substantial increases in rhodochrosite saturation. These

633 models translate to ferruginous marine conditions, implying a significantly less oxidizing
634 environment is required to develop carbonate-hosted sedimentary Mn enrichments than
635 previously recognized. Specifically, our findings suggest primary Mn-carbonates may
636 originate from waters containing 5 μM dissolved O_2 or less, and do not require the burial
637 of precursor Mn-oxides in sediments.

638 Instead of representing diagenetic organic carbon respiration, the negative carbon
639 isotope composition commonly observed in Mn-carbonates might also be imparted by
640 organic carbon remineralization or CH_4 oxidation occurring in the water column. Hence
641 some sedimentary Mn enrichments may develop where processes operating in low O_2
642 environments including sulfur cycling, microaerophilic Fe-oxidation, or anoxygenic
643 photosynthesis co-occur with a basin lysocline. This interpretation may reconcile
644 inconsistencies among paleoredox proxies in environments where Mn-enriched sediments
645 are encountered.

646

647

648 **Acknowledgements**

649 We thank Andrey Bekker, Louis Derry, Frantz Ossa Ossa, and an anonymous reviewer
650 for suggestions that significantly improved this contribution. J. Barry Maynard
651 generously shared his compilation of manganese ore data. This study was supported by
652 an NSF awards (EAR-1660691, EAR-1660761, EAR-1660873) to ES, CW, and SK, and
653 by NSF-1338322 to AM and others. ES's contribution benefited from support of the Iowa
654 Space Grant Consortium under NASA Award No. NNX16AL88H. We thank Duncan

655 Widman, Paige Bauer, Raisa Islam, and Gabrielle Ledesma for field and laboratory
656 assistance.
657
658
659
660
661
662 **Figure and Table Captions**
663
664 Figure 1: Sedimentary manganese enrichments (SMEs) through geologic time in
665 comparison with redox indicators. Manganese data replotted from Maynard (2010),
666 expressed as metric tons Mn metal, including sub-economic and iron-formation hosted
667 deposits. a. Atmospheric O_2 from Lyons et al., 2014. b. All SMEs binned in 200 Myr
668 increments. c. Post-Neoproterozoic marine redox indicators including ocean anoxic
669 events (OAEs; stars) from Jenkyns (2010), and cumulative thickness of marine red beds
670 (MRBs), replotted from Song et al. (2017). d. Post-Neoproterozoic SMEs binned in 25
671 Myr increments.
672
673 Figure 2: Brownie Lake 2015-2017 water column profiles of (a) O_2, (b) dissolved iron
674 (Fe^{2+}), (c) dissolved manganese (Mn^{2+}), (d) SO_4^{2-} and total dissolved sulfide (ΣS^{2-}), (e)
675 dissolved inorganic carbon (DIC), (f) the carbon isotopic composition of DIC, (g)
676 dissolved methane (CH_4), and (h) the carbon isotopic composition of dissolved CH_4

677 (inset shows high values observed near the chemocline). Replotted from Lambrecht et al.
678 (2020).
679
680 Figure 3: (a) pH, (b) calcite solubility, and (c) rhodochrosite (rhod.), and siderite (sid.).
681 solubility in the Brownie Lake water column in 2017. (d) Detail of July 2017 phases
682 including pseudokutnohorite (pseudokut.). Saturation index (SI) = log(IAP/K_{sp}) where
683 IAP is the solution ion activity product and K_{sp} is the solubility constant of the given
684 mineral.
685
686 Figure 4: Brownie Lake particulate and water column data from 2018. (a) Brownie Lake
687 water column dissolved O_2 and Mn. (b) Concentrations of HCl-extractable Mn from
688 filtered particulates, sediment trap materials, and surface sediments. (c) Sediment trap
689 and surface sediment HCl-extractable Mn normalized to total Mn (Mn_T), and Mn/Al. (d)
690 X-ray diffraction patterns from 5 m sediment trap sample versus surface sediments. Note
691 the prominence of the calcite peak in the sediment trap at 5 m relative to surface
692 sediments, interpreted as evidence of water column calcite dissolution. XRD peak labels:
693 C = calcite, D = dolomite, F = feldspars, M = 2M muscovite, Q = quartz.
694
695 Figure 5: Sensitivity of BL carbonate mineral saturation. Cal = calcite (blue), Rhod =
696 rhodochrosite (black), and Sid = siderite (red). All changes expressed in terms of delta
697 Q/K where Q = IAP and K = given mineral solubility constant. All scenarios are plotted
698 in terms of a 15-day simulation and based on BL water chemistry as measured in July
699 2017 at 5.5 m (Table 1). See main text for example reactions. (a.) Scenario considering

700 aerobic respiration where O_2 and CO_2 are reacted in a 1:1 molar ratio. (b.) Methane
701 oxidation scenario where 2 moles of O_2 are consumed for every CO_2 produced. (c.)
702 Sulfate reduction scenario. (d.) Addition of calcite at 7 μmol/day scenario. (e-h.) The
703 combination of scenarios b-d. with varying temperature and pH. Note change in scale of
704 delta Q/K for g. and h. (i-l.) Scenarios combining b-d. adopting Brownie Lake dissolved
705 Fe, Mn, SO_4, and O_2 concentrations and assuming seawater composition and pH and
706 temperature of 25 C. (i.) Seawater with Brownie Lake July 2107 5.5 m concentrations of
707 Fe, Mn, SO_4 and O_2. (j.) Scenario as described in (i.) with dissolved Mn concentration
708 increased to 134 μM, the highest observed in our study. (k.) Scenario as described in (i.)
709 with dissolved Mn concentration increased to 200 μM. (l.) Scenario as described in (i.)
710 with Ca:Mn ratio set to 18, the lowest observed in our study.
711
712 Figure 6. Combined scenarios for methane oxidation, sulfate reduction, and calcite
713 addition (i.e. Figure 5 b-d) applied to rhodochrosite-saturated intervals in BL. Mineral
714 abbreviations and Q/K relationships as in Figure 5. Panels a-c with mineral precipitation
715 suppressed to assess changes in solubility. (a) May 2017 6 m, (b) July 2017 5.5 m, (c)
716 July 2017 6 m. Panels d-f display pH changes from each of the scenarios above. Panels g-
717 i display results from unsuppressed simulations where minerals are allowed to precipitate
718 at Q/K = 1 and accumulate in the system, with mineral concentrations shown in μmoles.
719 Panels j-l display pH evolution of unsuppressed scenarios g-i.
720
721 Figure 7: Models for the genesis of sediment manganese enrichments (SMEs). Relative
722 water column composition of $\delta^{13}C_{DIC}$ and concentrations of O_2, Mn, Fe, and H_2S (if

applicable) shown to right. Each model assumes the presence of a basin lysocline coincident with a chemocline. Sources of Fe and Mn may include hydrothermal vents, springs (in lakes), or sediment porewater release. See main text for example reactions. (a) Carbonate model, based on the ferruginous setting described in this work. Manganese oxides may not be present if Mn-carbonate genesis rate exceeds rate of supply, and oxygenic photosynthesis may not have been active in earliest Archean examples. Calcite introduced to water column via littoral precipitation dissolves as it settles into the lysocline, where Mn-carbonates nucleate. Fe-rich overgrowths may precipitate (ppt) in deep waters if siderite saturation is exceeded. Fe-silicates such as greenalite may also co-precipitate in deep facies of Precambrian oceans (Jiang and Tosca, 2019). The composition of $\delta^{13}C_{DIC}$ is adopted from trends observed in Brownie Lake, but Precambrian oceans (pC) may not have hosted enriched $\delta^{13}C_{DIC}$ in deepest waters. Transgression is capable of shifting facies relationships to the left, creating contrasting sediment compositions. (b) Euxinic model, similar to the zoned model of Force and Cannon (1988) and a mechanism proposed by Herndon et al. (2018). Instead of carbonates, iron-sulfides dominate in deeper settings, but Mn-carbonates may still precipitate near the chemocline or if rates of $CaCO_3$ accumulation are high throughout the basin (e.g. Green Lake; Herndon et al., 2018). The $\delta^{13}C_{DIC}$ of deep water is shifted negative due to the predominance of sulfate reduction (Myrbo and Shapley, 2006). (c) The prevailing oxide model assumes that Mn-carbonates precipitate from a precursor oxide mineral (e.g. Calvert and Pederson, 1996). A deep water source of dissolved Mn is still implied. In Precambrian settings ferruginous conditions were likely dominant, but anoxic basins in the Phanerozoic are often interpreted as euxinic (H_2S rich). Both the

746 carbonate and euxinic model may produce SMEs in suboxic environments, but low
747 carbonate saturation or high rates of dissolved Mn upwelling may favor the oxide model.
748
749 Table 1: Inputs and reaction rates for carbonate modeling. Species concentrations (Conc.)
750 were measured from the BL water column except the seawater scenario, which adopted
751 values of major dissolved ion concentrations from seawater with the exception of Fe, Mn,
752 SO_4, and O_2. The Mn concentration in the seawater scenario is based on the lowest
753 observed BL Ca:Mn, with results shown in Figure 5 l. Reaction rates were determined by
754 dividing the measured concentrations by 15 days, the length of the scenario.
755
756
757
758
759
760
761
762
763
764
765
766
767
768
769

770 **References Cited (50/50)**

771

772 Assayag, N., Jézéquel, D., Ader, M., Viollier, E., Michard, G., Prévot, F., and Agrinier,
773 P., 2008. Hydrological budget, carbon sources and biogeochemical processes in Lac
774 Pavin (France): Constraints from $\delta^{18}O$ of water and $\delta^{13}C$ of dissolved inorganic carbon:
775 Applied Geochemistry, v. 23, no. 10, p. 2800-2816.

776

777 Berg, J. S., Jézéquel, D., Duverger, A., Lamy, D., Laberty-Robert, C., & Miot, J. (2019).
778 Microbial diversity involved in iron and cryptic sulfur cycling in the ferruginous, low-
779 sulfate waters of Lake Pavin. PLOS ONE, 14(2), e0212787.

780

781 Calvert, S.E., and Pedersen, T.F., 1996. Sedimentary geochemistry of manganese:
782 Implication for the environment of formation of manganiferous black shales. Economic
783 Geology v. 91, p. 36-47.

784

785 Clement, B.G., Luther, G.W. III, Tebo, B.M., 2009. Rapid, oxygen-dependent microbial
786 Mn(II) oxidation kinetics at sub-micromolar oxygen concentrations in the Black Sea
787 suboxic zone. Geochimica et Cosmochimica Acta, v. 73, p. 1878-1889.

788

789 Crowe, S., Katsev, S., Leslie, K., Sturm, A., Magen, C., Nomosatryo, S., Pack, M.,
790 Kessler, J., Reeburgh, W., and Roberts, J., 2011, The methane cycle in ferruginous Lake
791 Matano: Geobiology, v. 9, no. 1, p. 61-78.

792

793 Daye, M., Klepac-Ceraj, V., Pajusalu, M., Rowland, S., Farrell-Sherman, A., Beukes, N.,
794 Tamura, N., Fournier, G., and Bosak, T., 2019. Light-driven anaerobic microbial
795 oxidation of manganese. Nature, doi: 10.1038/s41586-019-1804-0.
796
797 Ettwig, K.F., Zhu, B., Speth, D., Keltjens, J.T., Jetten, M.S.M., and Kartal, B., 2016.
798 Archaea catalyze iron-dependent anaerobic oxidation of methane. Proceedings of the
799 National Academy of Sciences, v. 113, p, 12792-12796.
800
801 Farquhar, J., Zerkle, A.L., and Bekker, A., 2014. 6.4 - Geologic and geochemical
802 constraints on Earth's early atmosphere. Treatise on Geochemistry, v. 6, p. 91-138.
803
804 Force, E.R., and Cannon, W.F., 1988. Depositional model for shallow-marine manganese
805 deposits around black shale basins. Economic Geology, v. 83, p. 93-117.
806
807 Gumsley, A.P., Chamberlain, K.R., Bleeker, W., Soderlund, U., de Kock, M., Larsson,
808 E.R., and Bekker, A., 2017. Timing and tempo of the Great Oxidation Event. Proceedings
809 of the National Academy of Sciences, v. 114, p. 1811-1816.
810
811 Hausler, K., Dellwig, O., Schnetger, B., Feldens, P., Leipe, T., Moros, M., Pollehne, F.,
812 Schonke, M., Wegwerth, A., and Arz, H.W., 2018. Massive Mn carbonate formation in
813 the Landsort Deep (Baltic Sea): hydrographic conditions, temporal succession, and Mn
814 budget calculations. Marine Geology v. 395, p. 260-270.
815

816 Havig, J.R., Hamilton, T.L., McCormick, M., McClure, B., Sowers, T., Wegter, B., and
817 Kump, L.R., 2017. Water column and sediment stable carbon isotope biogeochemistry of
818 permanently redox-stratified Fayetteville Green Lake, New York, USA. Limnology and
819 Oceanography, v. 63, p, 570-587.
820
821 Herndon, E.M., Havig, J.R., Singer, D.M., McCormick, M.L., and Kump, L.R., 2018.
822 Manganese and iron geochemistry in sediments underlying the redox-stratified
823 Fayetteville Green Lake. Geochimica et Cosmochimica Acta, v. 231, p. 50-63.
824
825 Jenkyns, H.C., 2010. Geochemistry of ocean anoxic events. Geochemistry, Geophysics,
826 Geosystems, v. 11, doi:10.1029/2009GC002788.
827
828 Jiang, C.Z., and Tosca, N.J., 2019. Fe(II)-carbonate precipitation kinetics and the
829 chemistry of anoxic ferruginous seawater. Earth and Planetary Science Letters, v. 506, p.
830 231-242.
831
832 Johnson, J.E., Webb, S.M., Thomas, K., Ono, S., Kirschvink, J.L., and Fischer, W.W.,
833 2013. Manganese-oxidizing photosynthesis before the rise of cyanobacteria. Proceedings
834 of the National Academy of Sciences, v. 110, p. 11238-11243.
835
836 Johnson, J.E., Webb, S.M., Ma, C., and Fischer, W.W., 2016. Manganese mineralogy and
837 diagenesis in the sedimentary rock record. Geochimica et Cosmochimica Acta, v. 173, p.
838 210-231.

839

840 Jones, C., Crowe, S.A., Sturm, A., Leslie, K.L., MacLean, L.C.W., Katsev, S., Henry, C.,
841 Fowle, D.A., and Canfield, D.E., 2011. Biogeochemistry of manganese in ferruginous
842 Lake Matano, Indonesia: Biogeosciences v. 8., p. 2977-2991

843

844 Kirschvink, J.L., Gaidos, E.J., Bertani, E.L., Beukes, N.J., Gutzmer, J., Maepa, L.N., and
845 Steinberger, R.L., 2000. Paleoproterozoic snowball Earth: Extreme climatic and
846 geochemical global change and its biological consequences. Proceedings of the National
847 Academy of Sciences, v. 97, p. 1400-1405.

848

849 Lambrecht, N., Wittkop, C., Katsev, S., Fakhraee, M., and Swanner, E.D. Geochemical
850 characterization of two ferruginous meromictic lakes in the Upper Midwest, USA, 2018.
851 Journal of Geophysical Research – Biogeosciences, doi:10.1029/2018JG004587.

852

853 Lambrecht, N., Katsev, S., Wittkop, C., Hall, S.J., Sheik, C.S., Picard, A., Fakhraee, M.,
854 and Swanner, E.D., 2020. Biogeochemical and physical controls on methane fluxes from
855 two ferruginous meromictic lakes. Geobiology, v. 18, p. 54-69, doi: 10.1111/gbi.12365.

856

857 Lantink, M.L., Oonk, P.B.H., Floor, G.H., Tsikos, H., and Mason, P.R.D., 2018. Fe
858 isotopes of a 2.4 Ga hematite-rich IF constrain marine redox conditions around the GOE.
859 Precambrian Research, v. 305, p. 218-235.

860

861 Lliros, M., Garcia-Armisen, T., Darchambeau, F., Morana, C., Triado-Margarit, X.,
862 Inceoglu, O., Borrego, C.M., Bouillon, S., Servais, P., Borges, A.V., Descy, J-P.,
863 Canfield, D.E., and Crowe, S.A., 2015. Pelagic photoferrotrophy and iron cycling in a
864 modern ferruginous basin. Scientific Reports, doi: 10.1038/srep13803.
865
866 Lyons, T.W., Reinhard, C.T., and Planavsky, N.J., 2014. The rise of oxygen in Earth's
867 early ocean and atmosphere: Nature, v. 506, p. 307-315.
868
869 Maynard, J.B., 2010. The chemistry of manganese ores through time: A signal of
870 increasing diversity of Earth-surface environments. Economic Geology, v. 105, p. 535-
871 552.
872
873 Michaelis, W., Seifert, R., Nauhaus, K., Treude, T., Thiel, V., Blumenberg, M., Knittel,
874 K., Gieseke, A., Peterknecht, K., Pape, T., Boetius, A., Amann, R., Jorgensen, B.B.,
875 Widdel, F., Peckman, J., Pimenov, N.V., and Gulin, M.B., 2002. Microbial reefs in the
876 Black Sea fueled by anaerobic oxidation of methane. Science, v. 297, p. 1013-1015.
877
878 Morse, J.W., Arvidson, R.S., and Luttge, A., 2007. Calcium carbonate formation and
879 dissolution. Chemical Reviews, v. 107, p, 342-381.
880
881 Mucci, A., 2004. The behavior of mixed Ca-Mn carbonates in water and seawater:
882 Controls of manganese concentrations in marine porewaters. Aquatic Geochemistry, v.
883 10, p 139-169.

884

885 Myrbo, A., and Shapley, M., 2006, Seasonal water-column dynamics of dissolved
886 inorganic carbon stable isotopic compositions ($\delta^{13}C_{DIC}$) in small hardwater lakes in
887 Minnesota and Montana: Geochimica et Cosmochimica Acta, v. 70, no. 11, p. 2699-
888 2714.

889

890 Neubert, N., Nagler, T.F., and Bottcher, M.E., 2008. Sulfidity controls molybdenum
891 isotope fractionation into euxinic sediments: evidence from the modern Black Sea.
892 Geology v. 36, p. 775-778.

893

894 Nuhfer, E.B., Anderson, R.Y., Bradbury, J.P., and Dean, W.E., 1993, Modern
895 sedimentation in Elk Lake, Clearwater County, Minnesota, in Bradbury, J.P., and Dean,
896 W.E., eds., Elk Lake, Minnesota: Evidence for rapid climate change in the North-Central
897 United States: Boulder, Colorado, Geological Society of America Special Paper 276, p.
898 75-96.

899

900 Okita, P.M., 1992. Manganese carbonate mineralization in the Molgano District, Mexico.
901 Economic Geology, v. 87, p. 1345-1366.

902

903 Ossa Ossa, F., Hofmann, A., Wille, M., Spangenberg, J.E., Bekker, A., Poulton, S.W.,
904 Eickmann, B., and Schoenberg, R., 2018a. Aerobic iron and manganese cycling in a
905 redox-stratified Mesoarchean epicontinental sea. Earth and Planetary Science Letters, v.
906 500, p. 28-40.

907

908 Ossa Ossa, F., Eickmann, B., Hofmann, A., Planavsky, N.J., Asael, D., Pambo, F., and
909 Bekker, A., 2018b. Two-step deoxygenation at the end of the Paleoproterozoic
910 Lomagundi Event. Earth and Planetary Science Letters, v. 486, p. 70-83.
911
912 Oswald, K., Jegge, C., Tischer, J., Berg, J., Brand, A., Miracle, M.R., Soria, X., Vicente,
913 E., Lehmann, M.F., Zopfi, J., and Schubert, C.J., 2016. Methanotrophy under versatile
914 conditions in the water column of the ferruginous meromictic Lake La Cruz (Spain).
915 Frontiers in Microbiology, v. 7, doi:10.3389/fmicb.2016.01762.
916
917 Pingitore, N.E., Eastman, M.P., Sandidge, M., Oden, K., and Freiha, B., 1988. The
918 coprecipitation of Manganese(II) with calcite: an experimental study. Marine Chemistry,
919 v. 25, p. 107-120.
920
921 Planavsky, N.J., Asael, D., Hofmann, A., Reinhard, C.T., Lalonde, S.V., Knudsen, A.,
922 Wang, X., Ossa Ossa, F., Pecoits, E., Smith, A.J.B., Beukes, N.J., Bekker, A., Johnson,
923 T.M., Konhauser, K.O., Lyons, T.W., and Rouxel, O.J., 2014. Evidence for oxygenic
924 photosynthesis half a billion years before the Great Oxidation Event. Nature Geoscience,
925 v. 7, p. 283-286.
926
927 Planavsky, N.J., Slack, J.F., Cannon, W.F., O'Connell, B., Isson, T.T., Asael, D.,
928 Jackson, J.C., Hardisty, D.S., Lyons, T.W., and Bekker, A., 2018. Evidence for episodic

oxygenication in a weakly redox buffered deep mid-Proterozoic ocean. Chemical Geology, v. 483, p. 581-594.

Poulton, S.W., Fralick, P.W., and Canfield, D.E., 2010. Spatial variability in oceanic redox structure 1.8 billion years ago. Nature Geoscience, v. 3, p. 486-490.

Rincon-Tomas, B., Khonsari, B., Muhlen, D., Wickbold, C., Schafer, N., Hause-Reitner, D., Hoppert, M., and Reitner, J., 2016. Manganese carbonates as possible biogenic relics in Archean settings. International Journal of Astrobiology, v. 15, p. 219-229.

Roy, S., 2006. Sedimentary manganese metallogenesis in response to the evolution of the Earth system. Earth-Science Reviews, v. 77, p. 273-305.

Song, H., Jiang, G., Poulton, S.W., Wignall, P.B., Tong, J., Song, H., An, Z., Chu, D., Tian, L., She, Z., and Wang, C., 2017. The onset of widespread marine red beds and the evolution of ferruginous oceans. Nature Communications, doi: 10.1038/s41467-017-00502-x

Stevens, L.R., Ito, E., and Olson, D.E.L., 2000. Relationship of Mn-carbonates in varved lake-sediments to catchment vegetation in Big Watab Lake, MN, USA. Journal of Paleolimnology, v. 24, p. 199-211.

951 Sturm, A., Fowle, D.A., Jones, C., Leslie, K., Nomosatryo, S., Henry, C., Canfield, D.E.,
952 and Crowe, S.A., 2019. Rates and pathways of CH4 oxidation in ferruginous Lake
953 Matano, Indonesia. Geobiology, v. 17, p. 294-307.
954
955 Thamdrump, B., Fossing, H., and Jorgensen, B.B., 1994. Manganese, iron, and sulfur
956 cycling in a coastal marine sediment, Aarhus Bay, Denmark. Geochimica et
957 Cosmochimica Acta, v. 58, p. 5115-5129.
958
959 Tsikos, H., Matthews, A., Erel, Y., and Moore, J.M., 2010. Iron isotopes constrain
960 biogeochemical redox cycling of iron and manganese in a Paleoproterozoic stratified
961 basin. Earth and Planetary Science Letters, v. 298, p. 125-134.
962
963 Van Cappellen, P., Viollier, E., Roychoudhury, A., Clark, L., Ingall, E., Lowe, K., and
964 Dichristina, T., 1998. Manganese and Iron at the oxic-anoxic transition of a stratified
965 marine basin (Orca Basin, Gulf of Mexico). Environmental Science and Technology, v.
966 32, p. 2931-2939.
967
968 Walter, X.A., Picazo, A., Miracle, M.R., Vicente, E., Camacho, A., Aragno, M., and
969 Zopfi, J., 2014. Phototrophic Fe(II)-oxidation in the chemocline of a ferruginous
970 meromictic lake. Frontiers in Microbiology, doi: 10.3389/fmicb.2014.00713.
971
972 Winter, B. L., and Knauth, L. P., 1992, Stable isotope geochemistry of cherts and
973 carbonates from the 2.0 Ga Gunflint Iron Formation: implications for the depositional

974 setting, and the effects of diagenesis and metamorphism: Precambrian Research, v. 59,
975 no. 3, p. 283-313.
976
977 Wittkop, C., Teranes, J., Lubenow, B., and Dean, W.E., 2014, C- and O-stable isotopic
978 signatures of methanogenesis, temperature, and water column stratification in Holocene
979 siderite varves. Chemical Geology, v. 389, p. 153-166.

Figure 1

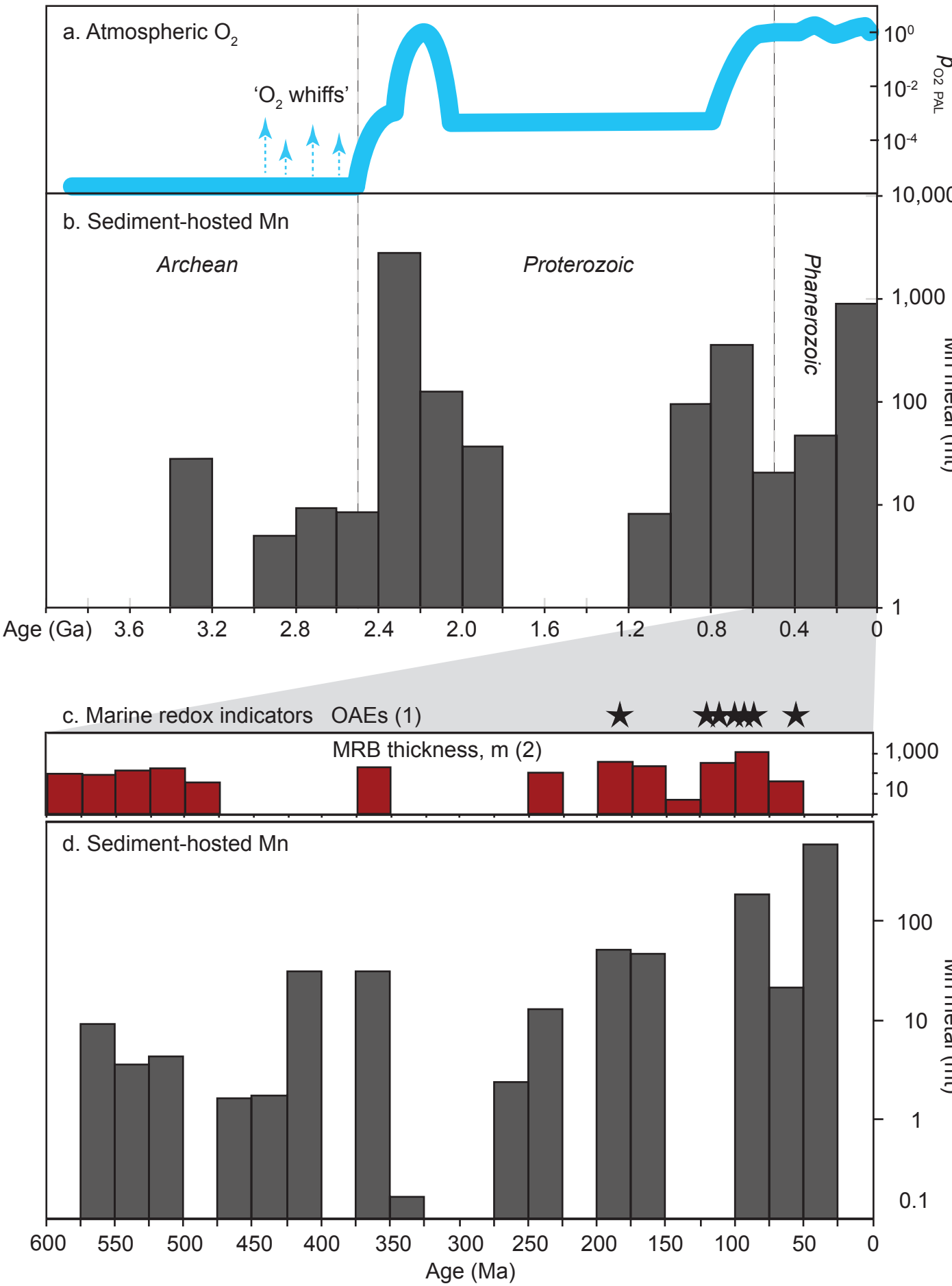
a. Atmospheric O_2
'O_2 whiffs'
10^0
10^{-2}
10^{-4}
$p_{O2\ PAL}$
10,000
b. Sediment-hosted Mn
Archean
Proterozoic
Phanerozoic
1,000
100
10
1
Mn metal (mt)
Age (Ga) 3.6 3.2 2.8 2.4 2.0 1.6 1.2 0.8 0.4 0
c. Marine redox indicators OAEs (1)
MRB thickness, m (2)
1,000
10
d. Sediment-hosted Mn
100
10
1
0.1
Mn metal (mt)
600 550 500 450 400 350 300 250 200 150 100 50 0
Age (Ma)

Figure 2

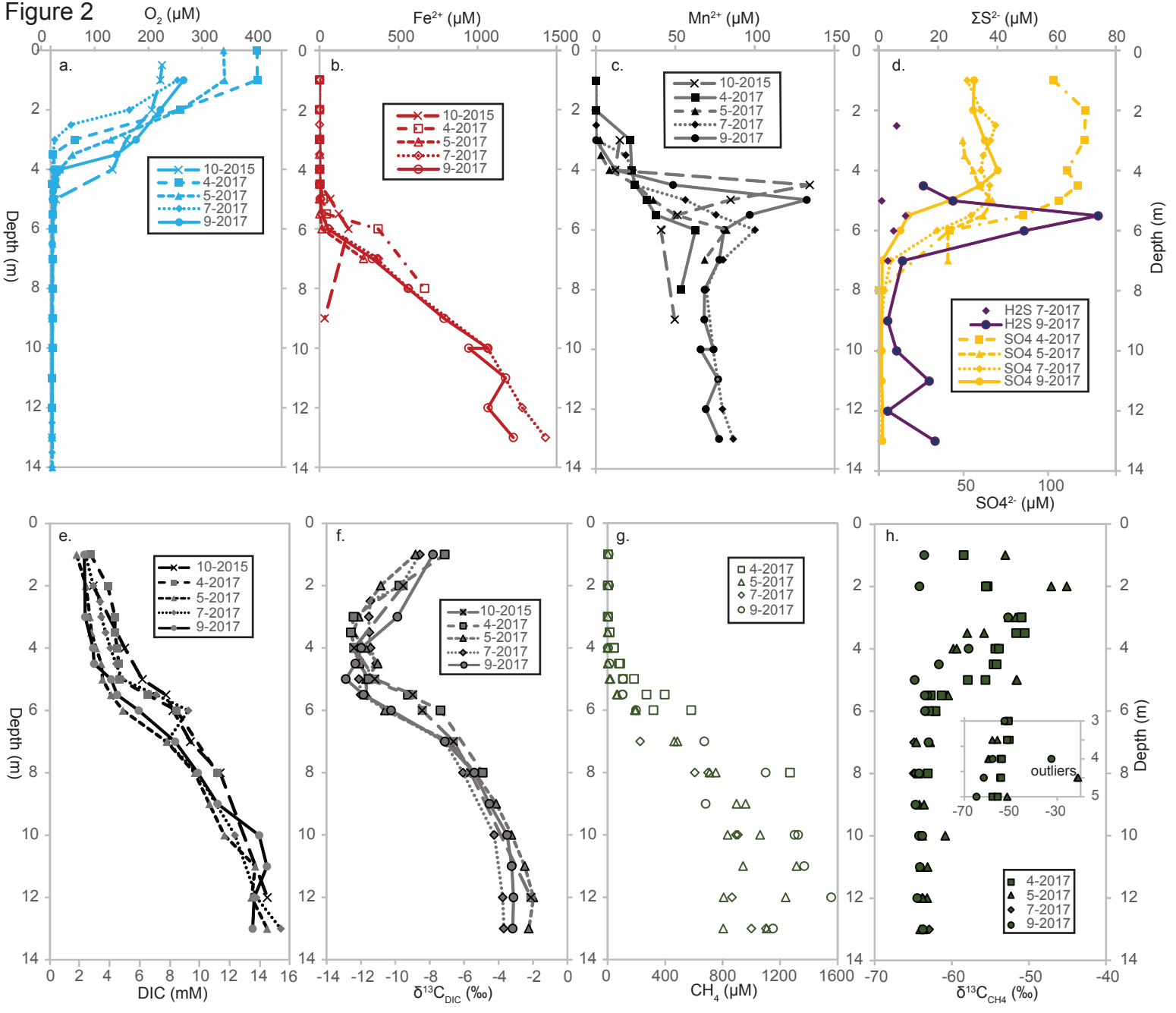
a.
O_2 (μM)
0 100 200 300 400
Depth (m)
10-2015
4-2017
5-2017
7-2017
9-2017
b.
Fe^{2+} (μM)
0 500 1000 1500
10-2015
4-2017
5-2017
7-2017
9-2017
c.
Mn^{2+} (μM)
0 50 100 150
10-2015
4-2017
5-2017
7-2017
9-2017
d.
ΣS2- (μM)
0 20 40 60 80
Depth (m)
H2S 7-2017
H2S 9-2017
SO4 4-2017
SO4 5-2017
SO4 7-2017
SO4 9-2017
50 100
$SO4^{2-}$ (μM)
e.
10-2015
4-2017
5-2017
7-2017
9-2017
Depth (m)
0 2 4 6 8 10 12 14 16
DIC (mM)
f.
10-2015
4-2017
5-2017
7-2017
9-2017
-14 -12 -10 -8 -6 -4 -2 0
$\delta^{13}C_{DIC}$ (‰)
g.
4-2017
5-2017
7-2017
9-2017
0 400 800 1200 1600
CH_4 (μM)
h.
outliers
-70 -50 -30
3 4 5
4-2017
5-2017
7-2017
9-2017
-70 -60 -50 -40
$\delta^{13}C_{CH4}$ (‰)
Depth (m)

Figure 3

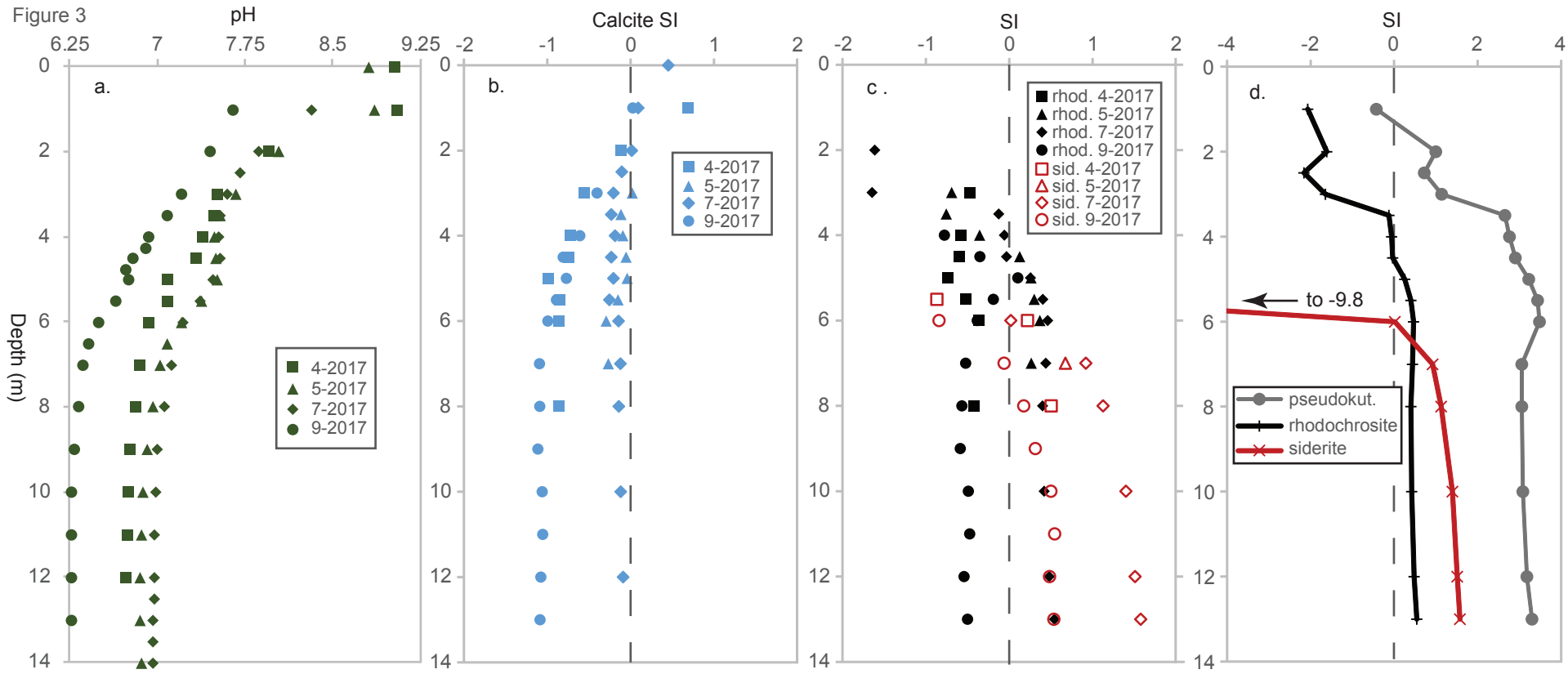
pH
6.25
7
7.75
8.5
9.25
a.
4-2017
5-2017
7-2017
9-2017
Depth (m)
0
2
4
6
8
10
12
14
Calcite SI
-2
-1
0
1
2
b.
4-2017
5-2017
7-2017
9-2017
SI
c .
rhod. 4-2017
rhod. 5-2017
rhod. 7-2017
rhod. 9-2017
sid. 4-2017
sid. 5-2017
sid. 7-2017
sid. 9-2017
SI
-4
-2
0
2
4
d.
to -9.8
pseudokut.
rhodochrosite
siderite

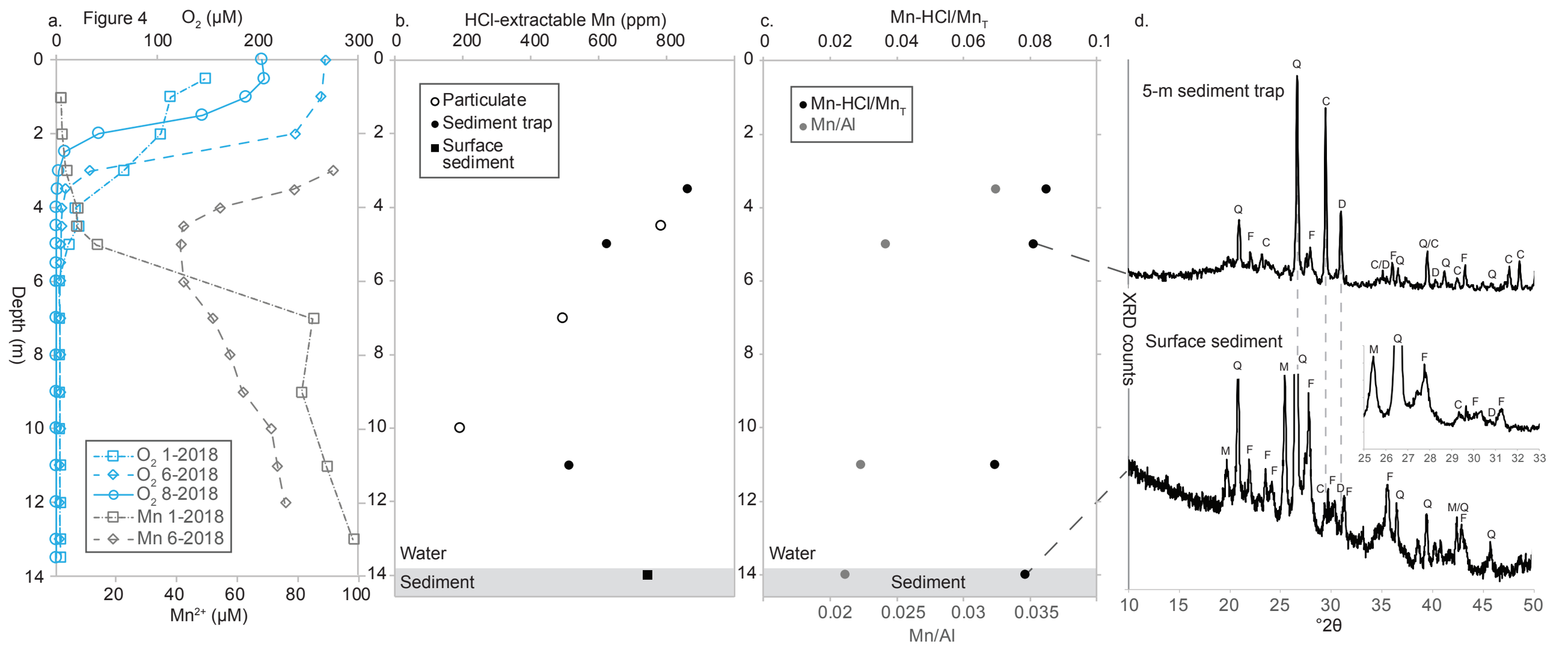
a.
Figure 4
O_2 (μM)
0
100
200
300
Depth (m)
0
2
4
6
8
10
12
14
O_2 1-2018
O_2 6-2018
O_2 8-2018
Mn 1-2018
Mn 6-2018
20
40
60
80
100
Mn^{2+} (μM)
b.
HCl-extractable Mn (ppm)
0
200
400
600
800
Particulate
Sediment trap
Surface sediment
Water
Sediment
c.
Mn-HCl/Mn_T
0
0.02
0.04
0.06
0.08
0.1
Mn-HCl/Mn_T
Mn/Al
Water
Sediment
0.02
0.025
0.03
0.035
Mn/Al
d.
5-m sediment trap
Surface sediment
XRD counts
Q
C
F
D
C/D
Q/C
M
M/Q
10
15
20
25
30
35
40
45
50
°2θ

Figure 5

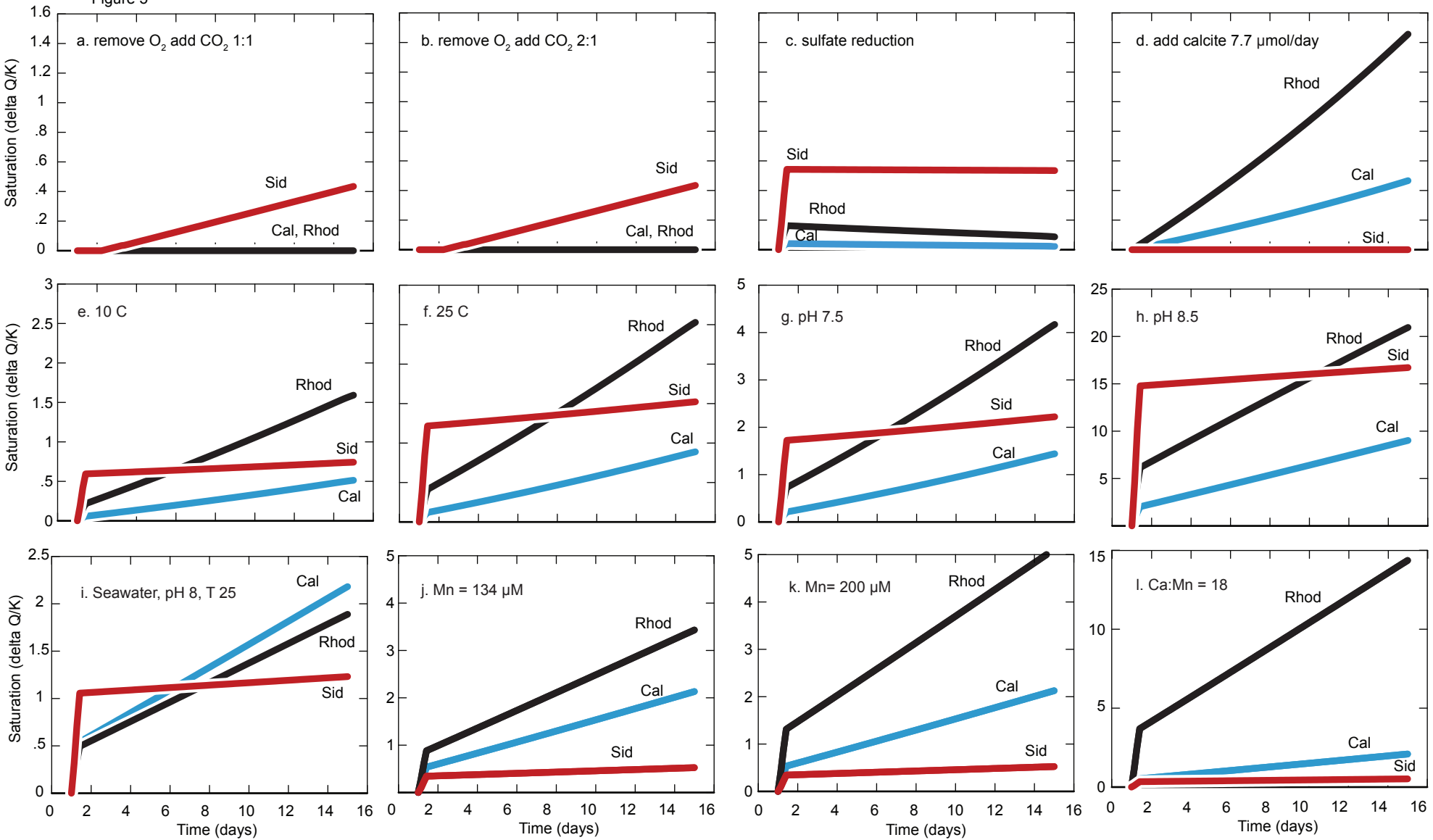
a. remove O_2 add CO_2 1:1
b. remove O_2 add CO_2 2:1
c. sulfate reduction
d. add calcite 7.7 µmol/day
e. 10 C
f. 25 C
g. pH 7.5
h. pH 8.5
i. Seawater, pH 8, T 25
j. Mn = 134 µM
k. Mn= 200 µM
l. Ca:Mn = 18
Rhod
Sid
Cal
Cal, Rhod
Saturation (delta Q/K)
Time (days)

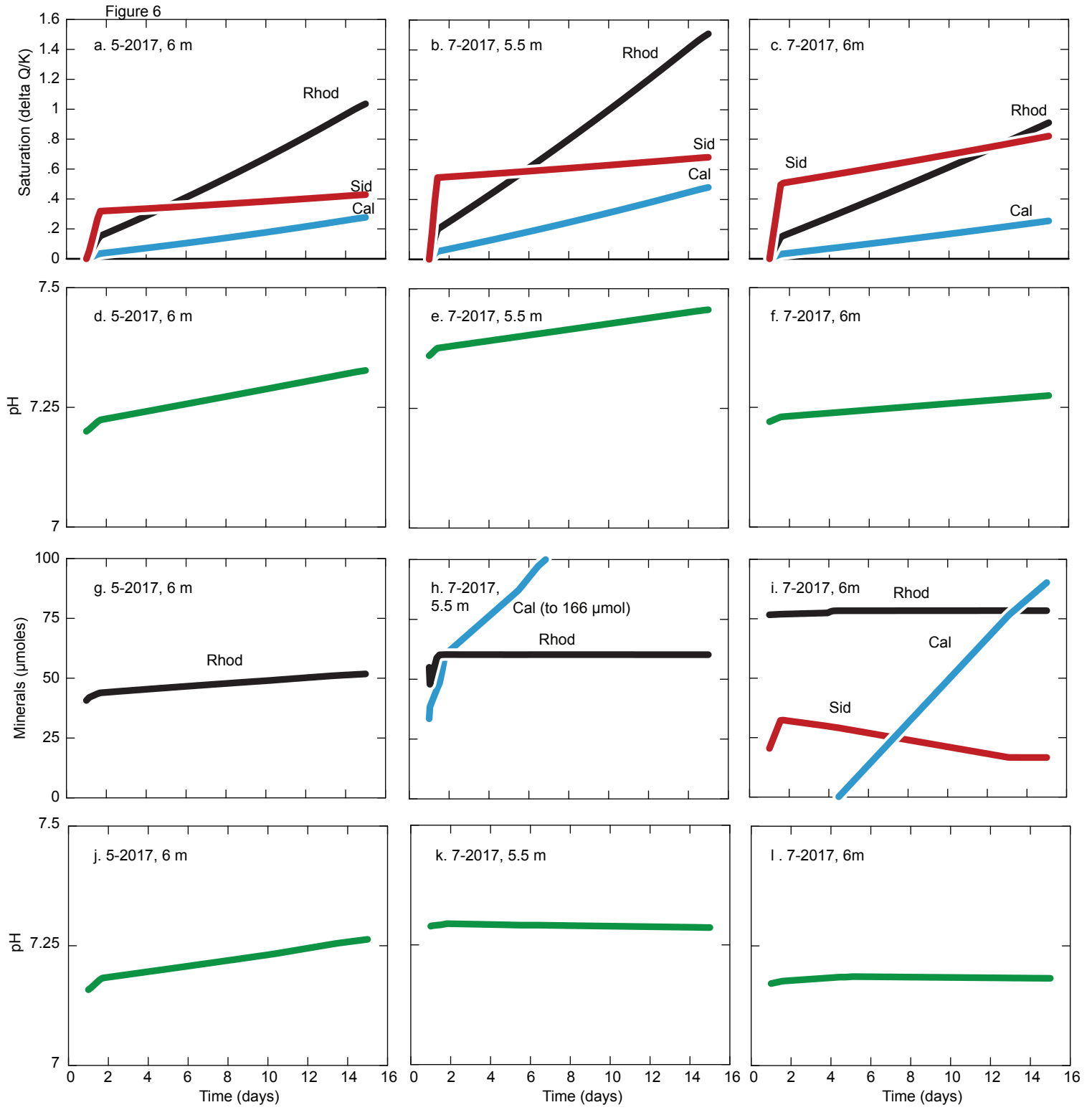
Figure 6
a. 5-2017, 6 m
b. 7-2017, 5.5 m
c. 7-2017, 6m
Saturation (delta Q/K)
Rhod
Sid
Cal
d. 5-2017, 6 m
e. 7-2017, 5.5 m
f. 7-2017, 6m
pH
g. 5-2017, 6 m
h. 7-2017, 5.5 m
Cal (to 166 µmol)
i. 7-2017, 6m
Minerals (µmoles)
j. 5-2017, 6 m
k. 7-2017, 5.5 m
l . 7-2017, 6m
Time (days)

Figure 7

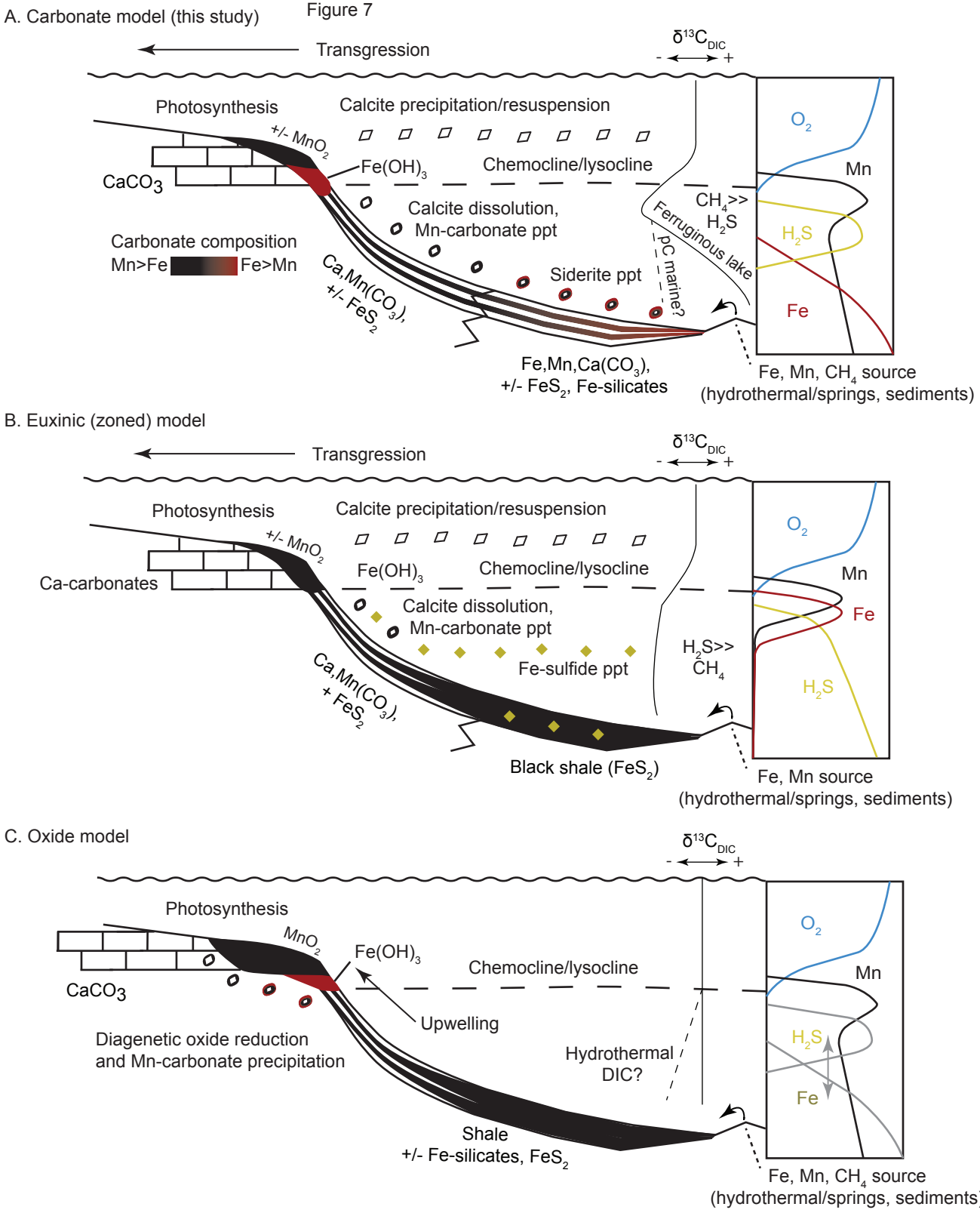
A. Carbonate model (this study)
Transgression
δ13CDIC
- +
Photosynthesis
+/- MnO2
Calcite precipitation/resuspension
Fe(OH)3
Chemocline/lysocline
CaCO3
Calcite dissolution,
Mn-carbonate ppt
Carbonate composition
Mn>Fe
Fe>Mn
Ca,Mn(CO3),
+/- FeS2
Siderite ppt
CH4>>
H2S
Ferruginous lake
pC marine?
O2
Mn
H2S
Fe
Fe,Mn,Ca(CO3),
+/- FeS2, Fe-silicates
Fe, Mn, CH4 source
(hydrothermal/springs, sediments)
B. Euxinic (zoned) model
Transgression
δ13CDIC
- +
Photosynthesis
+/- MnO2
Calcite precipitation/resuspension
Fe(OH)3
Chemocline/lysocline
Ca-carbonates
Calcite dissolution,
Mn-carbonate ppt
Ca,Mn(CO3),
+ FeS2
Fe-sulfide ppt
H2S>>
CH4
O2
Mn
Fe
H2S
Black shale (FeS2)
Fe, Mn source
(hydrothermal/springs, sediments)
C. Oxide model
δ13CDIC
- +
Photosynthesis
MnO2
Fe(OH)3
Chemocline/lysocline
CaCO3
Upwelling
Diagenetic oxide reduction
and Mn-carbonate precipitation
Hydrothermal
DIC?
O2
Mn
H2S
Fe
Shale
+/- Fe-silicates, FeS2
Fe, Mn, CH4 source
(hydrothermal/springs, sediments)

Wittkop et al., in press. Table 1.

Interval	May 2017 6m		July 2017 5.5m		July 2017 6m		Seawater / July 2017 5.5m	
Species	Conc.	Units	Conc.	Units	Conc.	Units	Conc.	Units
Al^{3+}	-	-	0.371	µmol/L	0.408	µmol/L	0.371	µmol/L
$B(OH_4)^-$	2.868	µmol/L	6.753	µmol/L	6.660	µmol/L	6.753	µmol/L
Ca^{2+}	1906	µmol/L	1933	µmol/L	2008	µmol/L	10.28	mmol/kg
Cr^{3+}	0.019	µmol/L	0.019	µmol/L	0.038	µmol/L	0.019	µmol/L
Fe^{2+}	15.40	µmol/L	11.76	µmol/L	63.57	µmol/L	11.76	µmol/L
K^+	206.20	µmol/L	192.16	µmol/L	220.52	µmol/L	10.2	mmol/kg
Mg^{2+}	720.6	µmol/L	749.3	µmol/L	795.8	µmol/L	52.8	mmol/kg
Mn^{2+}	82.15	µmol/L	75.45	µmol/L	99.99	µmol/L	571	µmolar
Na^+	15046	µmol/L	14720	µmol/L	16666	µmol/L	469	mmol/kg
Cl^-	20164	µmol/L	16931	µmol/L	18482	µmol/L	546	mmol/kg
Br^-	33.79	µmol/L	3.755	µmol/L	5.006	µmol/L	0.84	mmol/kg
SO_4^{2-}	40.60	µmol/L	54.13	µmol/L	34.35	µmol/L	54.13	µmol/L
HPO_4^{2-}	0.293	µmol/L	0.592	µmol/L	0.907	µmol/L	0.592	µmol/L
O_2	4.1	µmol/L	3.13	µmol/L	2.8	µmol/L	3.1	µmol/L
H^+	7.2	pH	7.36	pH	7.22	pH	8	pH
HCO_3^-	4.4	mM	6.5	mM	8.4	mM	1.77	mmol/kg
NO_3^-	-	-	-	-	0.1290	µmol/L	-	-
T	7.58	°C	8.33	°C	7.58	°C	25	°C
Ca/Mn	23		26		20		18	
Mn/Fe	5.3		6.4		1.6		49	
Reactant	Rate (µM/day)		Rate (µM/day)		Rate (µM/day)		Rate (µM/day)	
O_2	-0.27		-0.21		-0.19		-0.21	
CO_2	0.14		0.10		0.09		0.10	
Calcite	7.70		7.70		7.70		7.70	
SO^{42-}	-2.71		-3.61		-2.29		-3.61	
H_2S	2.71		3.61		2.29		3.61	
HCO_3^-	5.41		7.22		4.58		7.22	